A Novel PCB-Embedded Coupled Inductor Structure for a 20-MHz Integrated Voltage Regulator

Feiyang Zhu, *Graduate Student Member, IEEE*, and Qiang Li, *Member, IEEE*

***Abstract*— As power demands of processors in portable electronics continuously grow, the voltage regulator (VR) for the processor is expected to be efficient and miniaturized. Compared with a discrete VR solution, the integrated voltage regula-tor (IVR) can be placed very close to the processor to support dynamic voltage and frequency scaling, which helps significantly reduce the power consumption of the processor. One of the major challenges for IVRs is the high-frequency inductor development. This article proposes a novel, negative-coupled inductor structure with a simple core structure. The coupling coefficient of the proposed structure can be adjusted by changing the inductor winding pattern without modifying the magnetic core structure. The method for adjusting the coupling and the flux distribution in the magnetic core are analyzed in detail. A multiphase integrated inductor is proposed to further enhance the inductor performance by flux cancellation. A printed circuit board (PCB)-embedded four-phase inductor is designed, manufactured, and tested at 20 MHz. The device integrates four inductors into a single-piece magnetic core, featuring an inductance density of 9.7 nH/mm^3, a dc resistance (DCR) of 3.1 m• per phase, and a thickness of 0.54 mm with high current-handling ability.**

***Index Terms*— Integrated voltage regulator (IVR), magnetic integration, multiphase coupled inductor, printed circuit board (PCB) embedding.**

I. Introduction

Due to its high efficiency and simple structure, multi-phase buck topology has been widely used in voltage regulator (VR) design for use in powering the processors of portable devices. However, passive components, such as inductors and capacitors, occupy considerable space on the motherboard because of the relatively low switching frequency of VRs in today's commercial products (e.g., below 5 MHz in smartphones). An integrated voltage regulator (IVR) [1]–[4] is proposed to shrink the size of passive components and save space significantly by operating the switching frequency in tens of megahertz. Furthermore, fine-grained dynamic voltage and frequency scaling (DVFS) [5]–[7] becomes possible by locating the IVR closer to the processor because of a smaller size of the IVR, thus dramatically reducing the energy consumption of processors.

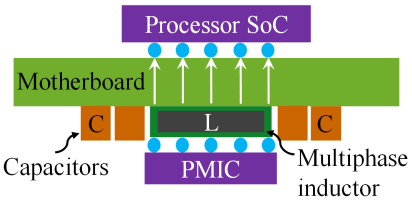

Fig. 1. 3-D IVR with a five-phase integrated inductor.

One of the key bottlenecks for IVR development is the high-frequency inductor design and integration. Various high-frequency inductor structures are demonstrated in [11]–[38]; the single-phase, non-coupled inductor is the most popular structure. A 3-D IVR with a five-phase integrated inductor was proposed in [14], as shown in Fig. 1. The inductor and power management integrated circuit (PMIC) are placed right beneath the processor to deliver the power in a shorter distance and to save a considerable footprint occupied by discrete inductors on the motherboard. This inductor structure not only integrates five inductors into one magnetic core, but also achieves an ultralow dc resistance (DCR) due to a very simple winding structure. Meanwhile, most of the high-frequency magnetic flux is well-confined in the magnetic core, due to the non-air-gap design. However, the core loss of this inductor is relatively large due to its one-turn structure. The coupling between any two phases is very weak, and it is still a non-coupled inductor structure.

In comparison with non-coupled inductors, a small steady-state current ripple and fast transient response as well as a smaller inductor size can be achieved by using a negative-coupled inductor [8]. A two-phase negative-coupled inductor with a stripline core structure was proposed in [16] and [17]. The dc flux in the core is decreased, and a higher saturation current can be realized due to negative coupling; however, its single-turn structure makes it challenging to design a large inductance in a small form factor. Additionally, the coupling coefficient of this structure may not be flexibly adjusted since the leakage flux flows through the air. A five- or eight-phase coupled inductor structure was proposed in [3] and [23]. In this structure, each inductor is

Manuscript received 9 March 2022; accepted 16 July 2022. Date of publication 27 July 2022; date of current version 6 December 2022. Some ideas shared in this article were presented at ECCE 2021. The title there was "A Novel PCB-Embedded Coupled Inductor Structure for Integrated Voltage Regulator." This work was supported by National Science Foundation, under Award 1653156. Recommended for publication by Associate Editor Jose A. Cobos. *(Corresponding author: Feiyang Zhu.)*

The authors are with the Center for Power Electronics Systems, Virginia Polytechnic Institute and State University, Blacksburg, VA 24061 USA (e-mail: feiyz94@vt.edu).

Color versions of one or more figures in this article are available at https://doi.org/10.1109/JESTPE.2022.3194133.

Digital Object Identifier 10.1109/JESTPE.2022.3194133

coupled with the other two adjacent inductors, resulting in a better performance as compared with the two-phase coupled inductor; however, the long winding path of each inductor causes a large DCR. A discrete magnetic core is needed for each inductor which increases the fabrication burden and complexity. A four-phase coupled inductor with a single-piece magnetic core was presented in [28]. Although four inductors are integrated into one magnetic core in this structure, the inherent reluctance difference in the magnetic paths results in asymmetrical coupling, which will create a phase current ripple variation and a larger output voltage ripple [9], [10]. Therefore, a multiphase coupled inductor structure featuring symmetrical coupling, a small DCR, and low profile with integrated magnetics needs to be developed for the IVR design.

A two-phase coupled inductor structure for high-current point-of-load applications was proposed in [40] and [41]. This structure can realize a large inductance density, regardless of the magnetic core thickness due to the lateral flux pattern [39], making it suitable for a low-profile design. Negative coupling helps reduce the dc flux in the core and shrink the core volume. To realize a reasonable coupling coefficient under different load currents, the slots in the magnetic core have to be filled with a different magnetic material. Adding additional magnetic material into the slots increases the fabrication cost and may not be practical when the inductor is embedded into a printed circuit board (PCB).

In this study, a novel multiphase coupled inductor structure with integrated magnetics for a 3-D IVR is proposed, based on the concept of a lateral flux inductor [39]. By changing the inductor winding distribution, the coupling coefficient of the proposed structure is controlled in a desirable region without sacrificing inductor footprint or increasing fabrication cost, as compared with the structures in [40] and [41]. At the same time, this structure still carries the traditional benefits of neg-ative coupling, including dc flux cancellation in the magnetic core, good circuit performance due to a small phase current ripple, and fast transient speed. Furthermore, the proposed structure integrates multiple inductors into one magnetic core to further improve the inductor performance by utilizing flux cancellation and to reduce the fabrication cost.

This article is organized as follows. The working principles and limitations of the multiturn coupled inductor structure with a lateral flux pattern are reviewed in Section II. Then, the coupling coefficient and the flux distribution of the proposed two-phase coupled inductor structure are analyzed in detail in Section III. To further enhance the inductor performance, a multiphase integrated inductor structure is proposed in Section IV. Then, a design example of a PCB-embedded inductor with the proposed inductor structure is presented to demonstrate the benefits of this structure. Finally, experimental results are presented in Section V.

II. Review of Multiturn Coupled Inductor Structure With a Lateral Flux Pattern

The two-phase coupled inductor structures with a lateral flux pattern [40], [41] are shown in Fig. 2. In this example, each inductor has four vias and three surface windings. The cross

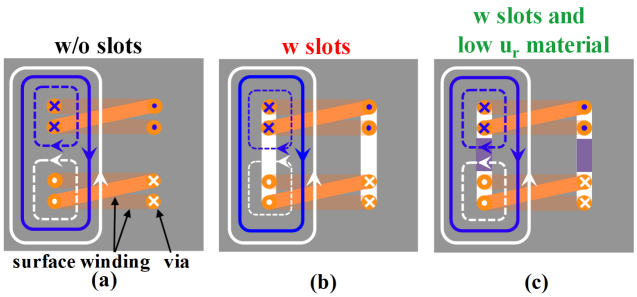

Fig. 2. Multiturn coupled inductor structures: (a) inductor without slots in the magnetic core; (b) inductor with slots; and (c) inductor with slots filled by low-permeability magnetic material (purple) (orange: top surface windings; faded orange: bottom surface windings).

on the via exhibits the current flowing into the paper, and the current flowing out of the paper is depicted by the dot. The white and blues lines represent the flux paths of two inductors, respectively. For the structure in Fig. 2(a), the mutual flux path and leakage flux path of each inductor are represented by solid lines and dashed lines, respectively. Negative coupling is formed due to the opposite direction of mutual fluxes from two inductors. It is seen that the leakage fluxes of two inductors have the same direction in the core area between two inductors. Therefore, the dc flux density in this area will be much lower at light load than at heavy load. Due to the non-air-gap design, the permeability of this structure varies with load currents. Consequently, the permeability in the core area between two inductors will become larger at light load, resulting in more leakage flux flowing through this area. Thus, the coupling coefficient of this structure decreases from heavy load to light load as shown in Fig. 3(a). In addition to the coupling coefficient change, the self-inductance of this structure increases from the heavy load to the light load, due to the permeability variation, as shown in Fig. 3(b). The steady-state inductance and transient inductance of the coupled inductor are calculated as follows:

$$L_{ss} = L_{self}\frac{1-\alpha^2}{1+\alpha\frac{D}{1-D}} \quad (1)$$

$$L_{tr} = L_{self}(1+\alpha) \quad (2)$$

where α is the coupling coefficient, L_{self} is the self-inductance, L_{ss} is the steady-state inductance, and L_{tr} is the transient inductance. The L_{ss} and L_{tr} of the structure in Fig. 2(a) are shown in Fig. 3(c) and (d), respectively. As shown, the large self-inductance and the small coupling coefficient at light load result in a large L_{ss}; thus, higher light-load efficiency is achieved. However, the large L_{tr} at light load causes a large voltage spike during the load transient [40].

To improve the transient performance, a modified structure is proposed in [40], as shown in Fig. 2(b). By adding two slots in the magnetic core, the reluctance of the leakage flux path barely varies with load currents due to the air gap created by the slots; hence, a large, constant coupling coefficient is achieved, as shown in Fig. 3(a). Meanwhile, a constant self-inductance is realized as a result of the strong dc flux cancellation effect. Therefore, the L_{tr} of this structure is controlled at a small value under different load currents, as shown in Fig. 3(d). However, the strong coupling coefficient

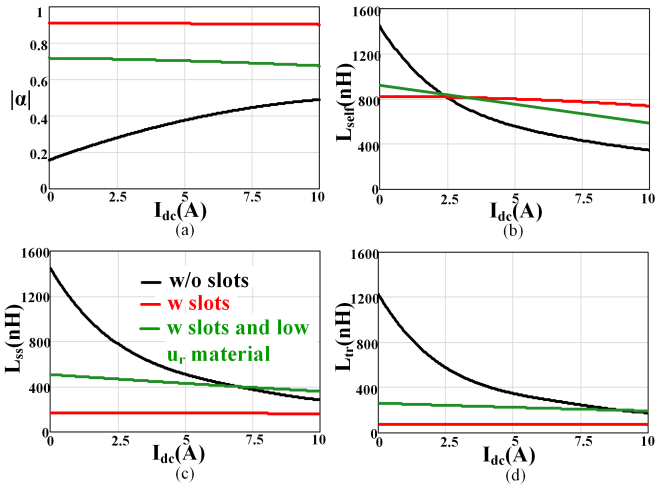

Fig. 3. Coupling and inductance comparison between different inductor structures with a given inductor volume: (a) coupling coefficient; (b) self-inductance; (c) steady-state inductance; and (d) transient inductance [black: inductor without slots in Fig. 2(a); red: inductor with slots in Fig. 2(b); and green: inductor with slots filled by low-permeability magnetic material in Fig. 2(c)].

(close to one) of this structure together with a smaller self-inductance makes the L_{ss} drop to a much smaller value, especially at light load, as compared with that of the structure without slots.

To achieve a larger L_{ss} and a constant L_{tr} over a wide load current range without increasing the inductor volume, Hou *et al.* [41] proposed applying a different magnetic material into the slots, as shown in Fig. 2(c). The low-permeability magnetic material creates more leakage flux and ensures the coupling coefficient not too strong. Due to the constant permeability property of this additional material, a constant and reasonable coupling coefficient is realized, as shown in Fig. 3(a). Then, a larger L_{ss} is obtained, as compared with that of the inductor with slots. At the same time, the L_{tr} is still kept at a small value under different load currents, as shown in Fig. 3(d). However, the fabrication complexity and cost are increased by the extra low-permeability material in the slots. For IVR applications, the required width and length of the slots could be very small in order to achieve a compact design, and it may not be practical to add additional magnetic materials into the slots. To resolve this issue, Section III proposes a novel coupled inductor structure to achieve a good performance without adding any additional magnetic material.

III. Proposed Two-Phase Coupled Inductor Structure

A. Proposed Coupled Inductor Structure

The proposed series asymmetrical coupled inductor (SACL) is shown in Fig. 4(a). In this example, each inductor is seen as a three-turn inductor. Instead of making all three windings from each inductor be located in the same pair of slots [such as the winding arrangement in Fig. 2(b)], the number of windings in each core of each inductor is different. For example, there are two windings in the left core and one winding in the other core for inductor L_1. The equivalent circuit model of SACL is shown in Fig. 4(b). Each inductor consists of two separate inductors in each core, as follows:

$$L_1 = L_{1a} + L_{1b} \tag{3a}$$

$$L_2 = L_{2a} + L_{2b} \tag{3b}$$

where L_{1a} is the inductance of L_1 in the left core, L_{1b} is the inductance of L_1 in the right core, L_{2a} is the inductance of L_2 in the left core, and L_{2b} is the inductance of L_2 in the right core. In each core, there is

$$\begin{bmatrix} v_{1a} \\ v_{2a} \end{bmatrix} = \begin{bmatrix} L_{1a} & M_{12a} \\ M_{12a} & L_{2a} \end{bmatrix} \begin{bmatrix} \frac{di_1}{dt} \\ \frac{di_2}{dt} \end{bmatrix} \tag{4a}$$

$$\begin{bmatrix} v_{1b} \\ v_{2b} \end{bmatrix} = \begin{bmatrix} L_{1b} & M_{12b} \\ M_{12b} & L_{2b} \end{bmatrix} \begin{bmatrix} \frac{di_1}{dt} \\ \frac{di_2}{dt} \end{bmatrix} \tag{4b}$$

where v_{1a}, v_{1b}, v_{2a}, and v_{2b} are voltages across L_{1a}, L_{1b}, L_{2a}, and L_{2b}, and i_1, and i_2 are inductor currents of L_1 and L_2. Also, we have

$$v_1 = v_{1a} + v_{1b} \tag{5a}$$

$$v_2 = v_{2a} + v_{2b}. \tag{5b}$$

It is assumed that a strong coupling is formed between the two inductors from L_1 and L_2 in each core by ignoring the fluxes flowing through the air slots. Then,

$$L_{1a} = L_{2b} = \frac{4}{R_{\text{core}}} \tag{6a}$$

$$L_{1b} = L_{2a} = \frac{1}{R_{\text{core}}} \tag{6b}$$

$$M_{12a} = M_{12b} = -\frac{2}{R_{\text{core}}} \tag{6c}$$

where R_{core} is the equivalent reluctance in each core. Substituting (4) and (6) into (5) yields the following inductance matrix:

$$\begin{bmatrix} v_1 \\ v_2 \end{bmatrix} = \begin{bmatrix} \frac{5}{R_{\text{core}}} & -\frac{4}{R_{\text{core}}} \\ -\frac{4}{R_{\text{core}}} & \frac{5}{R_{\text{core}}} \end{bmatrix} \begin{bmatrix} \frac{di_1}{dt} \\ \frac{di_2}{dt} \end{bmatrix}. \tag{7}$$

Therefore, the inductances and coupling coefficient of this coupled inductor are expressed as follows:

$$L_{\text{self}} = \frac{5}{R_{\text{core}}} \tag{8a}$$

$$M = -\frac{4}{R_{\text{core}}} \tag{8b}$$

$$\alpha_{\max} = \frac{M}{L_{\text{self}}} = -0.8 \tag{8c}$$

where L_{self}, M, and $\alpha_{\max}$ are the self-inductance, mutual inductance, and the maximum coupling coefficient of this coupled inductor. Due to the special winding placement, the maximum coupling coefficient of SACL is always less than 0.8 even with air slots. The simulated flux density in the core and coupling coefficient are shown in Fig. 5. As expected, the coupling coefficient is controlled to be less than 0.8 without adding additional magnetic materials into the slots.

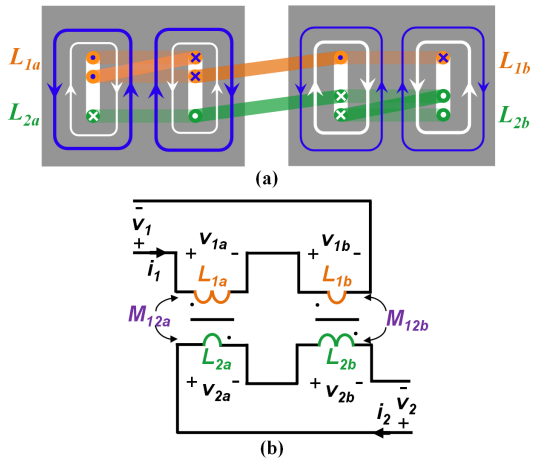

Fig. 4. SACL: (a) inductor structure and flux paths in the core and (b) equivalent circuit model (blue lines: flux paths of inductor L_1 and white lines: flux paths of inductor of L_2).

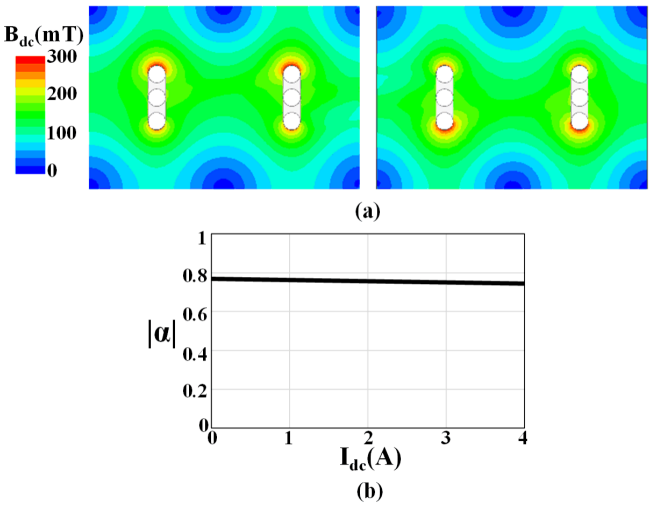

Fig. 5. Simulated flux density and coupling of SACL: (a) simulated flux density in the core and (b) simulated coupling coefficient.

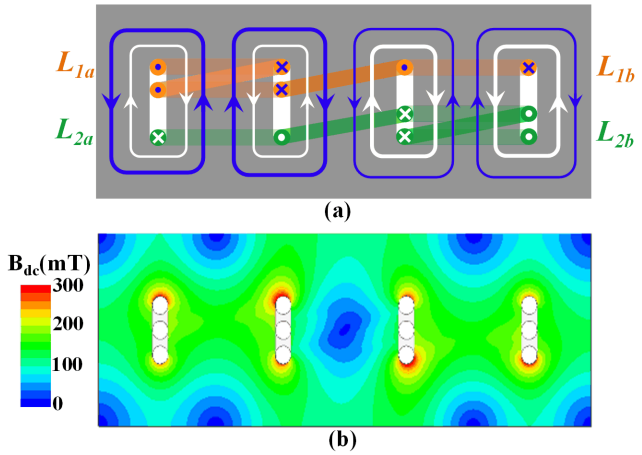

Fig. 6. ISACL: (a) inductor structure and (b) simulated flux density in the core.

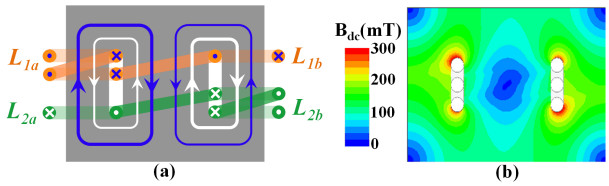

Fig. 7. MSACL: (a) inductor structure and (b) simulated flux density in the core.

TABLE I
SIMULATED INDUCTANCE AND COUPLING COEFFICIENT OF DIFFERENT COUPLED INDUCTOR STRUCTURES

Inductor structures	Lself(nH)	|M|(nH)	|α|
SACL	253.8	188.2	0.74
ISACL	253.6	185.6	0.73
MSACL	130.8	92.4	0.71
Proposed structure	128.2	92.8	0.72

The two separate magnetic cores in SACL can be further integrated into one single-piece core, and it becomes integrated series asymmetrical coupled inductor (ISACL) as shown in Fig. 6(a). In this structure, the dc fluxes from the two inductors are fully canceled in the middle of the core and result in a smaller dc flux density as shown in Fig. 6(b). Therefore, the fluxes of each inductor will flow in each half part of the core rather than flowing through the other half part of the core. Then, the coupling coefficient of ISACL should be the same as SACL. The simulated inductance and coupling coefficient of this structure are shown in Table I. It proves that the integration has no impact on the inductance and coupling of the proposed coupled inductor.

Although the proposed ISACL is a feasible solution to achieve a proper coupling coefficient, its inductor footprint is relatively large with a long winding path. To shrink the inductor size, the two sides of the core in ISACL are removed and it becomes the modified series asymmetrical coupled inductor (MSACL), as shown in Fig. 7. It is seen that the inductances and the core size of MSACL are both reduced to half of those in ISACL from Table I.

For MSACL, since the fluxes induced by the vias outside the core flow in the air, the inductance contributed by these vias is relatively small compared with the inductance generated in the core. Therefore, these vias can be removed to achieve a shorter winding length. To validate the idea, two single-phase inductor structures (only L_1 in the core) are compared first. The single-phase inductor of MSACL is shown in Fig. 8(a). The proposed single-phase inductor structure with a short winding length is shown in Fig. 8(b). Since the vias outside the core has little impact on the fluxes in the core, the flux distribution of two structures are almost the same. The simulated inductances of two structures are 94 and 92 nH, respectively. Although the proposed structure in Fig. 8(b) looks like a traditional inductor with the winding on the middle leg of an EE-typed core (a pair of E-shaped cores), it is indeed equivalent to the inductor in Fig. 8(a), where two windings on one side leg and the other winding on the other side leg from the inductance and flux distribution perspective.

Based on this understanding, the proposed coupled inductor with a shorter winding length is shown in Fig. 9. It is worth noting that this structure is equivalent to MSACL in

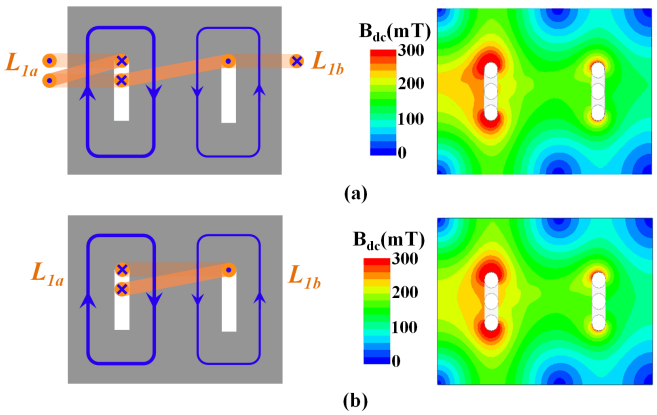

Fig. 8. Different single-phase inductor structures: (a) single phase of MSACL and its flux density distribution and (b) proposed single-phase inductor with a shorter winding length and its flux density distribution.

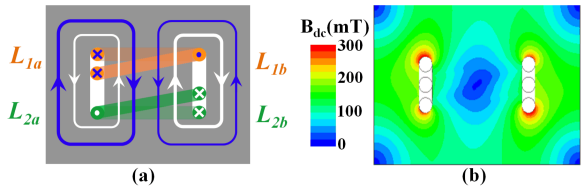

Fig. 9. Proposed coupled inductor structure: (a) inductor structure and (b) simulated flux density in the core.

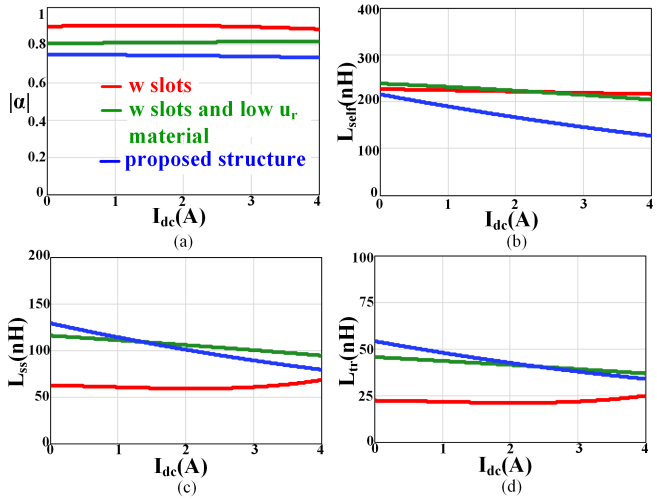

Fig. 10. Coupling and inductance comparison between different inductor structures with a given inductor volume: (a) coupling coefficient; (b) self-inductance; (c) steady-state inductance; and (d) transient inductance.

Fig. 7 from the inductance, coupling, and flux distribution perspective with a smaller DCR.

The coupling coefficient and inductance of different coupled inductor structures are compared, as shown in Fig. 10. The inductor volumes are kept the same for all cases. The coupling coefficient and self-inductance are obtained from Maxwell simulation by using the method in [44]. Then, L_{ss} and L_{tr} are calculated based on (1) and (2). From Fig. 10, it is seen that the proposed structure achieves larger equivalent inductances with a given inductor volume, as compared with the structure in Fig. 2(b). Therefore, with a given L_{ss}, the proposed structure will have a thinner core thickness. Compared with the structure in Fig. 2(c), the proposed structure achieves a similar coupling coefficient and equivalent inductances with a shorter winding length and

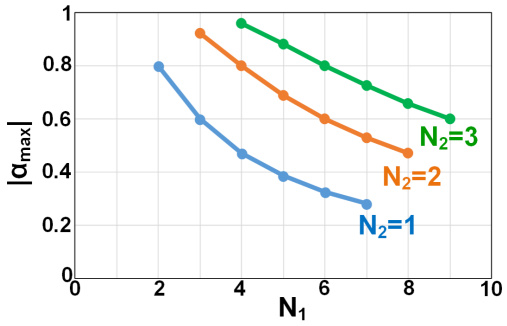

Fig. 11. Maximum coupling coefficient of different structures with different via distribution patterns.

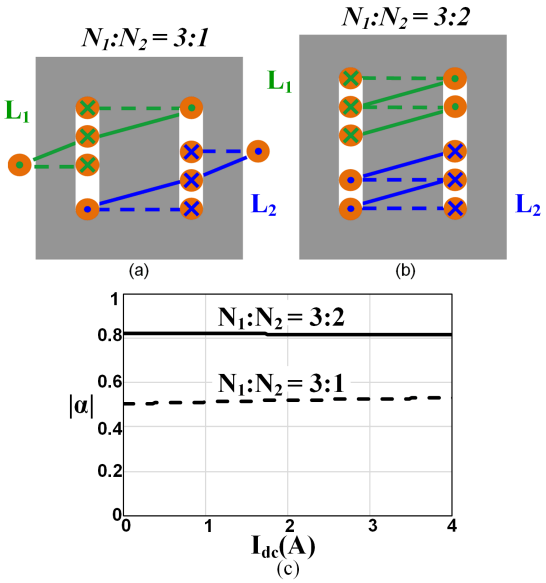

Fig. 12. Two different coupled inductor structures suitable for point-of-load applications and their coupling coefficients: (a) inductor with N_1: N_2 = 3:1; (b) inductor with N_1: N_2 = 3:2; and (c) simulated coupling coefficients of two structures (N_1: number of vias in the left slot of L_1; N_2: number of vias in the right slot of L_1).

a much simpler magnetic core structure without requiring additional low-permeability magnetic material. Furthermore, a small distance between the two inductors can be used in the proposed structure to achieve a smaller inductor size.

Based on the SACL concept, a coupled inductor family with a wide range of coupling and inductance can be achieved by changing the via distribution pattern in the slots. The number of vias in the left slot and that in the right slot of inductor L_1 are defined as N_1 and N_2, respectively. By following the previous analysis, the coupling coefficient is calculated as:

$$|\alpha_{max}| = \frac{2N_1N_2}{N_1^2 + N_2^2}. \tag{9}$$

Fig. 11 shows the maximum coupling coefficient of different inductor structures with different via distribution patterns. A wide range of coupling is achieved by different combina-tions of N_1 and N_2. The coupling coefficient increases when the difference between N_1 and N_2 becomes smaller. When N_1 = N_2, the coupling coefficient is one and it becomes a traditional multiturn coupled inductor. Fig. 12 shows two spe-cific inductor structures suitable for point-of-load applications. The maximum coupling coefficients of these two structures are −0.6 and −0.92, respectively. The simulated coupling

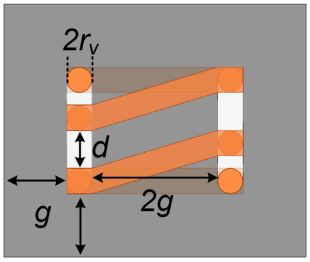

Fig. 13. Design parameters of the proposed two-phase coupled inductor.

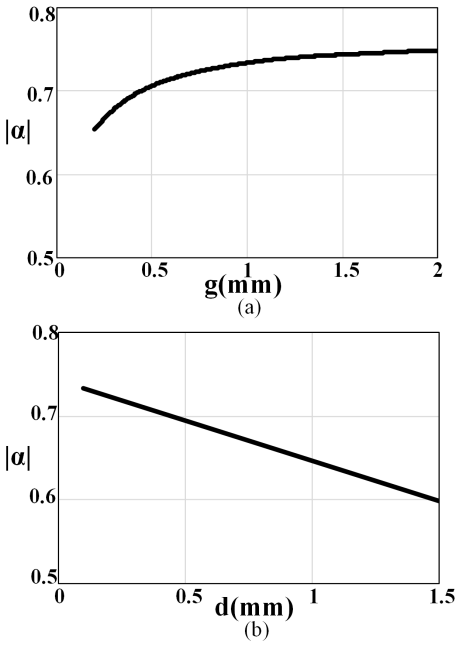

Fig. 14. Impact of design parameters on coupling: (a) impact of g (r_v = 0.15 mm, d = 0.1 mm, and h = 0.5 mm) and (b) impact of d (r_v = 0.15 mm, g = 1 mm, and h = 0.5 mm).

coefficients of these two structures are shown in Fig. 12(c). It is seen that their coupling coefficients are kept constant under different load currents.

B. Impact of Inductor Dimension on Coupling

To handle a large load current, the proposed coupled inductor structure in Fig. 9 is chosen for the inductor design due to its short winding length and small DCR. The impact of inductor parameters on the coupling will be discussed in this section. Fig. 13 shows the design parameters of the two-phase coupled inductor, which are via size r_v, core size g, the distance between the two inductors d, and core thickness h. For the basic design philosophy, r_v is determined by the maximum dc current, and h is constrained by the thickness requirement. Therefore, the remaining two variables, g and d, are swept, and their impact on the coupling is shown in Fig. 14. As g decreases, the coupling between the two inductors becomes weaker. The reason for this weakening is that the cross-sectional area of the magnetic core decreases with smaller values of g. Then, more flux will flow through the slots, thus making the coupling weaker. However, the coupling coefficient of this structure is always kept within a reasonable range under a wide range of g. With a given g, the coupling coefficient can be adjusted by d, as shown in Fig. 14(b). As expected, the coupling becomes stronger as the distance between the two inductors decreases.

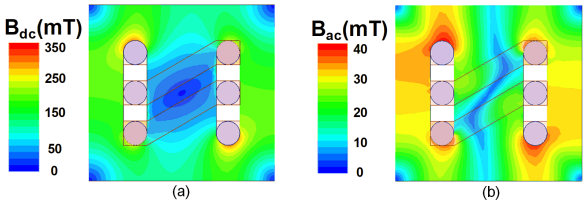

Fig. 15. Flux density distribution of the proposed structure: (a) dc flux density and (b) ac flux density.

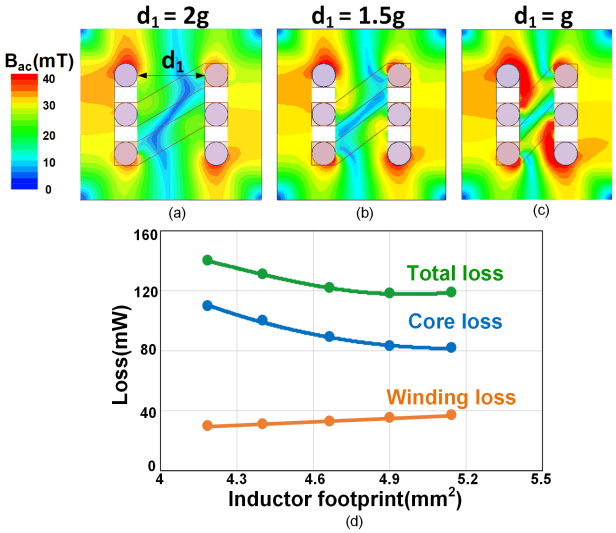

Fig. 16. Impact of d_1 on the flux density distribution and inductor losses: (a) d_1 = 2g; (b) d_1 = 1.5g; (c) d_1 = g; and (d) impact of d_1 on inductor loss and footprint.

C. Flux Distribution and Optimization

Due to the unique winding structure, the flux distribution in the magnetic core of the proposed structure needs further analysis. It has been shown that the directions of dc fluxes from two inductors are opposite due to negative coupling; furthermore, the dc flux is fully canceled in the middle part of the core, as shown in Fig. 9(a). Fig. 15 shows the simulated flux density in the core, obtained by Maxwell software. The metal-flake composite from TOKIN, Japan, [14] is used as the magnetic material. The simulation conditions are as follows: input voltage V_{in} = 3.8 V, output voltage V_o = 1 V, load current I_o = 3.75 A per phase, and switching frequency f_s = 20 MHz. The inductor parameters are as follows: r_v = 0.15 mm, d = 0.2 mm, g = 0.45 mm, and h = 0.5 mm. It is seen that the middle area of the core has the lowest dc flux density value. Due to the non-air-gap design, a larger permeability and inductance can be realized by a smaller dc flux in the core. Hence, the inductance density of this structure is boosted by the help of negative coupling. The ac flux density is also smaller in the middle part of the core due to phase interleaving, as shown in Fig. 15(b). Then, we can further optimize the core utilization for this structure. The

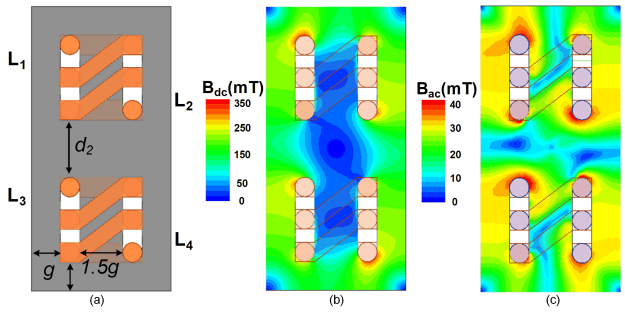

Fig. 17. (a) Proposed four-phase integrated inductor structure. (b) DC flux density in the core. (c) AC flux density in the core.

distance between the two slots is designated as d_1. Fig. 16 shows the flux density distribution and inductor losses per phase with different values of d_1. It is seen that a smaller d_1 reduces the unutilized core area, inductor footprint, and the length of surface windings with very little increased core loss. However, if d_1 is too small, a noticeably increased core loss occurs due to a much larger ac flux density in the middle area of the core. Therefore, the inductor structure in Fig. 16(b) can be chosen as an optimal point where a smaller inductor footprint is achieved with a negligible inductor loss increase. In this example, the structure in Fig. 16(b) realizes a 10% inductor footprint reduction compared with that of the original structure.

IV. PCB-Embedded Four-Phase Integrated Inductor

A. Proposed Four-Phase Integrated Inductor

A multiphase buck converter with multiple inductors is a necessity to handle the large power demand of processors in portable devices. Integrated magnetics normally outperforms discrete inductors because of a better core utilization and simple fabrication process. By merging two proposed two-phase coupled inductors into one magnetic core, a four-phase integrated inductor is proposed, as shown in Fig. 17(a). With the help of flux cancellation introduced by the integrated magnetics, both dc and ac flux densities in the area between the two inductor units are smaller, as compared with the discrete version. The optimal distance between the two inductor units, named d_2, is evaluated as shown in Fig. 18. The simulation conditions and inductor parameters are the same as those in the two-phase case. It is seen that the core loss increases little as the unutilized core area and inductor footprint are reduced at first. On the other hand, a much smaller d_2 value causes a considerable increased ac flux density and core loss. The design case in Fig. 18(b) is chosen considering the tradeoff between loss and footprint, where a 5% inductor footprint reduction is achieved with a slight increased inductor loss.

B. PCB-Embedded Integrated Inductor Design

For the inductor integration method, it can be classified into two major categories: silicon-wafer-level integration or package-level integration, such as the PCB embedding method. To meet the large load current requirement, the proposed

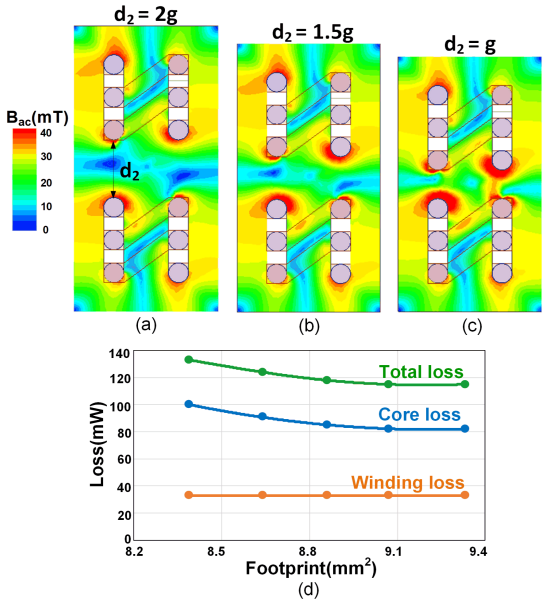

Fig. 18. Impact of d_2 on the flux distribution and inductor losses: (a) $d_2 = 2g$; (b) $d_2 = 1.5g$; (c) $d_2 = g$; and (d) impact of d_2 on inductor loss and footprint.

inductor structure is designed and demonstrated with the PCB-embedding technology. The design point of $V_{in} = 3.8$ V and $V_o = 1$ V is chosen according to the specifications in smartphones. The switching frequency is chosen as 20 MHz. The maximum load current of this four-phase integrated inductor is designed as 15 A. For the magnetic material, several studies [14], [42], [43] show that the metal-flake composite from TOKIN outperforms other materials because of its large permeability, small core loss density, and compatibility with the PCB manufacturing process. Another promising candidate is a new material from 3M, USA. Fig. 19 shows their high-frequency properties measured by an accurate magnetic characterization method targeted at tens of MHz [14], [45], [46]. Compared with the metal-flake composite material, the material from 3M has a lower core loss density but at the cost of a smaller relative permeability. Next, the PCB-embedded inductor performance based on these two materials is evaluated.

First, the two-phase coupled inductor design based on the metal-flake composite material is analyzed. The inductor loss is calculated by importing the measured material properties into Maxwell software. (A detailed description of this inductor loss calculation method is presented in [46].) A two-layer PCB is applied to embed the proposed inductor. The diameters of the copper filled vias are 0.15 mm. The surface windings are built by two copper layers. The thickness of the copper layers is 50 μm. The width of 0.65 mm is used for the slots. Fig. 20 shows the design curves with various inductances, core thickness, footprint, and inductor loss. The design points on each curve have the same L_{ss} value. For a fixed L_{ss}, a larger core thickness reduces the inductor footprint with a slight change of inductor loss. A larger core thickness helps lower the core loss as well as the inductor loss with a given footprint. To realize a small inductor loss and low profile, this

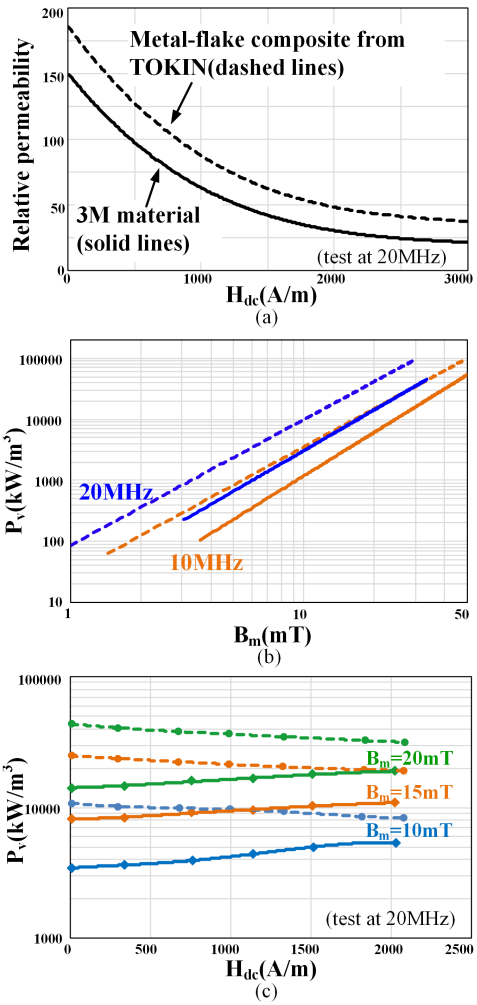

Fig. 19. Measured high-frequency properties of metal-flake composite from TOKIN (dashed lines) and 3M material (solid lines): (a) relative permeability versus H_{dc} at 20 MHz; (b) core loss density versus ac flux density; and (c) core loss density versus H_{dc} at 20 MHz.

two-phase coupled inductor is designed to have a footprint of 7 mm^2 and a core thickness of 0.3 mm. Table II shows the design results of the four-phase integrated inductor at 15-A load current after applying the previous design process of four-phase integrated inductor. The steady-state inductance is two times larger than the transient inductance to realize a small steady-state current ripple and fast transient speed at the same time. The total loss of this four-phase integrated inductor is 0.89 W with a footprint of 13.5 mm^2 and a core thickness of 0.3 mm. The DCR of each phase is only 2.8 m, due to a very simple winding structure. With the same inductor dimension, the design results using 3M material are listed in Table III. It is seen that the design with 3M material has a much smaller core loss since the 3M material has a lower core loss density. Although the winding loss increases a little due to a larger current ripple, the total inductor loss is reduced by 33% by using the 3M material, but at the cost of a 30% smaller steady-state inductance.

Finally, the bare inductors with metal-flake composite material and 3M material are embedded into a two-layer PCB. Fig. 21 shows the fabricated inductor device with a dimension

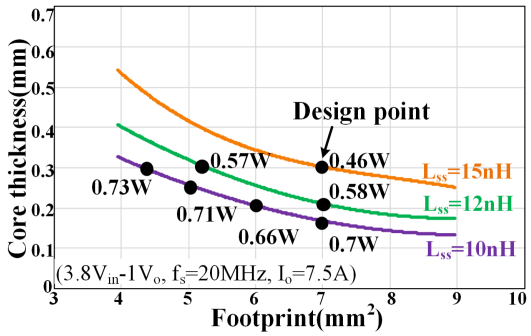

Fig. 20. Inductor size and loss evaluation of the two-phase coupled inductor based on the metal-flake composite material at 7.5 A load current.

TABLE II
DESIGN RESULTS OF FOUR-PHASE INTEGRATED INDUCTOR WITH METAL-FLAKE COMPOSITE MATERIAL

Parameters	Value
Steady-state inductance (L_{ss})	15 nH
Transient inductance (L_{tr})	7 nH
DC resistance (DCR)	2.8 mΩ
Core loss	0.68 W
Winding loss	0.21 W
Inductor total loss	0.89 W
Core thickness	0.3 mm
Core length	4.71 mm
Core width	2.86 mm

TABLE III
DESIGN RESULTS OF FOUR-PHASE INTEGRATED INDUCTOR WITH 3M MATERIAL

Parameters	Value
Steady-state inductance (L_{ss})	10.5 nH
Transient inductance (L_{tr})	5 nH
DC resistance (DCR)	2.8 mΩ
Core loss	0.35 W
Winding loss	0.25 W
Inductor total loss	0.6 W

(The inductor dimensions are the same as listed in TABLE I.)

of 5.21 × 3.36 × 0.54 mm^3. The inductor performance is tested experimentally in Section V.

V. EXPERIMENTAL RESULTS

A. Inductance Measurement

The inductance of the proposed inductor structure varies with different load currents due to the permeability change in the magnetic core. Hence, a specific inductance measurement method is proposed to characterize the inductance property of this coupled inductor under various load current conditions.

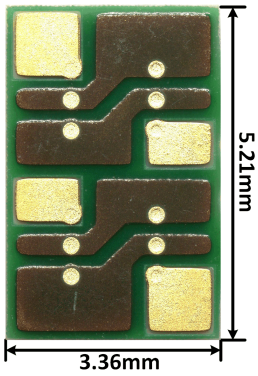

Fig. 21. Fabricated PCB-embedded four-phase inductor sample.

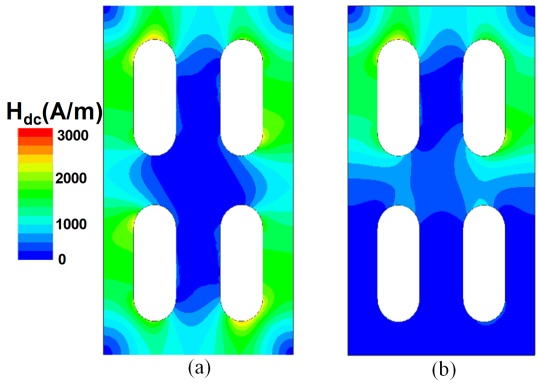

Fig. 22. Simulated dc magnetic field intensity in the core: (a) each inductor is applied with 3.75-A dc current and (b) only the upper two inductors are applied with 3.75-A dc current.

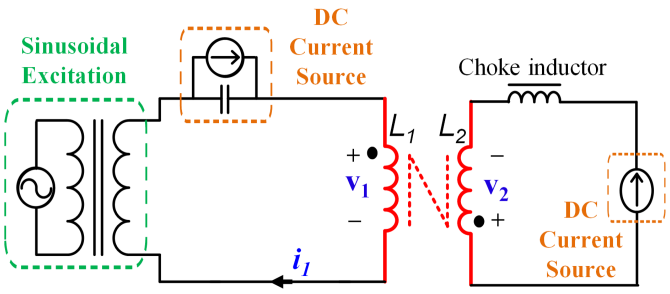

Fig. 23. Inductance measurement method for the proposed coupled inductor.

The simulated magnetic field intensity in the core under two different test settings is shown in Fig. 22. In the first test condition, all inductors are excited with a dc current; while the dc current is only applied to top two inductors in the second setting. Due to the weak coupling between top two inductors and the bottom ones, the current excitations in the bottom two inductors have little impact on the magnetic field intensity in the top part of the core. Hence, we can excite only top two inductor units with dc currents to measure its inductance.

The proposed inductance characterization method for this coupled inductor is shown in Fig. 23. Each inductor is excited with a dc current by a dc power supply. Only one inductor is excited with an ac excitation generated by a function generator together with a power amplifier. Due to the coupling, an ac voltage shows up on the other inductor. From the measured ac voltages and currents, the self-inductance and mutual inductor

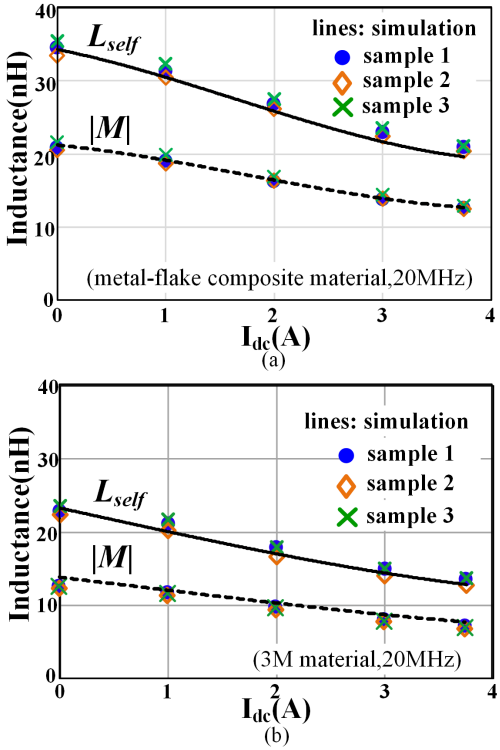

Fig. 24. Measured inductances of PCB-embedded inductor samples made by metal-flake composite material and 3M material at 20 MHz: (a) measured inductances with metal-flake composite material and (b) measured inductances with 3M material (points: measurement results of three different inductor samples; lines: simulation results).

of this coupled inductor can be obtained as

$$L_{\text{self}} = \frac{1}{2\pi f}\frac{V_1}{I_1} \tag{10}$$

$$|M| = \frac{1}{2\pi f}\frac{V_2}{I_1} \tag{11}$$

where V_1 and V_2 are the amplitudes of ac voltages on L_1 and L_2, respectively, I_1 is the amplitude of the ac current through L_1, and f is the test frequency of 20 MHz. The measured inductances of fabricated PCB-embedded inductor devices made by the metal-flake composite material and 3M material are shown in Fig. 24. It shows the measurements match well with the simulation. Hence, both magnetic materi-als are suitable for PCB-embedding process, and the inductor performance is not influenced by the PCB integration method. By using the four-wire Kelvin resistance measurement method, the measured DCR of each phase is 3.1 m, which is very close to the simulation value.

B. Thermal Test

Fig. 25 shows a four-phase buck converter board for the thermal test of the fabricated PCB-embedded inductor device. The high-frequency switching device, EPC2040 together with the gate driver PE29102 from pSemi, USA, is located on the top side of the board. There are output capacitors on the other side of the board. The inductor device is inserted into an opening in the middle of the board and soldered to the switching nodes and output capacitors by extra short wires. The thermal

TABLE IV
INDUCTOR PERFORMANCE COMPARISON

	[3]	[21]	[22]	[23]	[29]	[30]	[31]	[32]	[33]	This work
Substrate	Si	Si	Si	Si	PCB	PCB	PCB	PCB	PCB	PCB
number of phases	8, coupled	1	1	5, coupled	1	1	1	1	1	4, coupled
f_s(MHz)	100	>10	12	20	10	100	20	>10	>10	20
Footprint /phase(mm^2)	0.245	0.9	5.6	0.98	2.5	13	10.2	7.25	25	4.4
Height(mm)	/	/	0.28	0.09	/	0.56	2.3	1.46	0.35	0.54
L(nH)	5	120	85	12	33	31	150	52	5	23
R_{dc}(mΩ)	270	270	230	46	30	19	/	101	3.3	3.1
Inductance density (nH/mm^3)	/	/	54.2	136	/	4.3	6.4	4.9	0.6	9.7
Q ($\omega L/R_{ac}$)	/	14.5 @15MHz	14.3 @12.5MHz	/	8.5 @10MHz	8.1 @100MHz	38 @20MHz	23.3 @40MHz	15 @20MHz	16.3 @20MHz
L/R_{dc} (nH/mΩ)	0.02	0.44	0.37	0.26	1.1	1.63	/	0.51	1.5	7.4

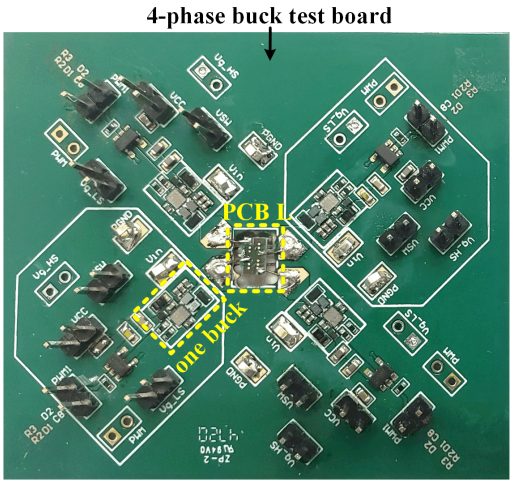

Fig. 25. Top view of the four-phase buck test board with a PCB-embedded inductor in the middle of the board.

test conditions are: V_{in} = 3.8 V, V_o = 1 V, f_s = 20 MHz, and 12-A-load current with natural convection. The temperature rises of the inductor with metal-flake composite material and 3M material are 55.4 °C and 49.4 °C, respectively, as shown in Fig. 26. It proves that the proposed inductor device is capable of delivering a large output current within a small form factor. Due to a smaller core loss, the temperature rise of the inductor with 3M material is 6 °C–8 °C lower than that of the inductor with metal-flake composite material over a wide load range, as shown in Fig. 26(c).

The inductor performance of prior arts and this work is compared in Table IV. Although the structures in [22] and [23] have a larger inductance density value, this work can achieve a much smaller DCR and a larger L/R_{dc} value. The work in [31] and [32] outperforms the proposed structure in terms of quality factor (Q). However, the proposed structure has a larger inductance density and a much smaller DCR value. As the functionality of the processor in portable electronics (e.g., smartphones) advances continuously, the current drawn from the processor is tens of amperes today and will be even higher in the future. The proposed structure is more suitable for this high-output current application due to its small DCR and large current-handling capability. Compared

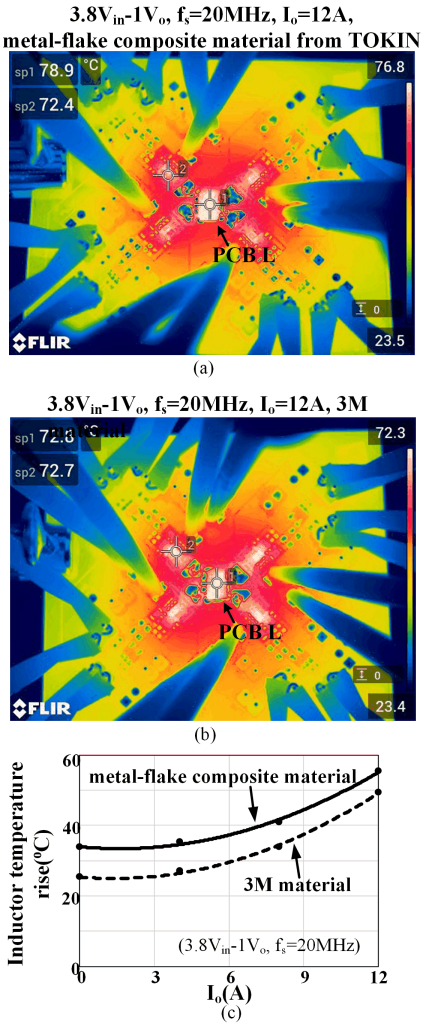

Fig. 26. Thermal test of PCB-embedded inductors: (a) thermal image of the PCB inductor with metal-flake composite material; (b) thermal image of the PCB inductor with 3M material (spot 1: inductor and spot 2: device); and (c) inductor temperature rise versus load current (solid line: metal-flake composite material and dashed line: 3M material).

with the work in [33], the proposed structure achieves a much larger inductance density value with a similar DCR and Q value. Furthermore, four inductors are integrated into one

single magnetic piece in this work for better performance and reducing the manufacture burden.

VI. Conclusion

In this article, a novel multiphase coupled inductor structure with integrated magnetics is proposed. By changing the inductor winding distribution pattern, the coupling coefficient of this structure is controlled in a desirable region with a simple core structure. A coupled inductor family with a wide range of coupling and inductance is proposed based on an equivalent circuit model. Because of negative coupling, the dc flux in the core is reduced. A small steady-state current ripple and fast transient speed are also realized from the perspective of circuit performance. The proposed structure integrates multiple inductors into one magnetic core, and the inductor performance is enhanced by flux cancellation. It is then embedded into a PCB with a detailed design process.

The experimental test results verify that the inductor performance is not influenced by the PCB integration method, and the proposed inductor device can support a large output current within a small form factor. In contrast to prior arts, the proposed inductor structure features a large inductance density and quality factor with a much smaller DCR, thus is seen as a promising candidate for IVR applications.

Acknowledgment

The authors would like to thank Dr. Fred C. Lee for his valuable and constructive discussion in this research work. They would also like to thank TOKIN and 3M for fabricating the bare inductor samples, and AT&S, Australia for manufacturing the printed circuit board (PCB)-embedded inductor devices.

References

[1] E. A. Burton *et al.*, "FIVR—Fully integrated voltage regulators on 4th generation Intelr Core™ SoCs," in *Proc. IEEE Appl. Power Electron. Conf. Expo. (APEC)*, Mar. 2014, pp. 432–439, doi: 10.1109/APEC.2014.6803344.

[2] G. Schrom *et al.*, "A 100 MHz eight-phase buck converter delivering 12 A in 25 mm^2 using air-core inductors," in *Proc. 22nd Annu. IEEE Appl. Power Electron. Conf. Expo.*, Feb. 2007, pp. 727–730, doi: 10.1109/APEX.2007.357595.

[3] N. Sturcken *et al.*, "A 2.5 D integrated voltage regulator using coupled-magnetic-core inductors on silicon interposer," *IEEE J. Solid-State Circuits*, vol. 48, no. 1, pp. 244–254, Jan. 2013, doi: 10.1109/JSSC.2012.2221237.

[4] P. Zou, Q. Xie, W. Song, Q. Jiang, Y. Lu, and B. Huang, "Powering 5G era computing platforms—The road toward integrated power delivery," in *Proc. 31st Int. Symp. Power Semiconductor Devices ICs (ISPSD)*, May 2019, pp. 1–6, doi: 10.1109/ISPSD.2019.8757569.

[5] T. Simunic, L. Benini, A. Acquaviva, P. Glynn, and G. De Micheli, "Dynamic voltage scaling and power management for portable systems," in *Proc. 38th Conf. Design Autom. (DAC)*, Jun. 2001, pp. 524–529.

[6] W. Kim, M. S. Gupta, G.-Y. Wei, and D. Brooks, "System level analysis of fast, per-core DVFS using on-chip switching regulators," in *Proc. IEEE 14th Int. Symp. High Perform. Comput. Archit.*, Feb. 2008, pp. 123–134, doi: 10.1109/HPCA.2008.4658633.

[7] S. Eyerman and L. Eeckhout, "Fine-grained DVFS using on-chip regulators," *ACM Trans. Archit. Code Optim. (TACO)*, vol. 8, no. 1, pp. 1–24, Apr. 2011.

[8] P.-L. Wong, P. Xu, B. Yang, and F. C. Lee, "Performance improvements of interleaving VRMs with coupling inductors," *IEEE Trans. Power Electron.*, vol. 16, no. 4, pp. 499–507, Jul. 2001, doi: 10.1109/63.931059.

[9] Y. Dong, F. C. Lee, and M. Xu, "Evaluation of coupled inductor voltage regulators," in *Proc. 23rd Annu. IEEE Appl. Power Electron. Conf. Expo.*, Feb. 2008, pp. 831–837, doi: 10.1109/APEC.2008.4522817.

[10] J. Li, A. Stratakos, A. Schultz, and C. R. Sullivan, "Using coupled inductors to enhance transient performance of multi-phase buck converters," in *Proc. 19th Annu. IEEE Appl. Power Electron. Conf. Expo.*, Feb. 2004, pp. 1289–1293, doi: 10.1109/APEC.2004.1295989.

[11] C. O. Mathúna, N. Wang, S. Kulkarni, and S. Roy, "Review of integrated magnetics for power supply on chip (PwrSoC)," *IEEE Trans. Power Electron.*, vol. 27, no. 11, pp. 4799–4816, Nov. 2012, doi: 10.1109/TPEL.2012.2198891.

[12] F. C. Lee and Q. Li, "High-frequency integrated point-of-load converters: Overview," *IEEE Trans. Power Electron.*, vol. 28, no. 9, pp. 4127–4136, Sep. 2013, doi: 10.1109/TPEL.2013.2238954.

[13] T. O'Donnell *et al.*, "Microfabricated inductors for 20 MHz DC–DC converters," in *Proc. 23rd Annu. IEEE Appl. Power Electron. Conf. Expo.*, Feb. 2008, pp. 689–693, doi: 10.1109/APEC.2008.4522796.

[14] D. Hou, F. C. Lee, and Q. Li, "Very high frequency IVR for small portable electronics with high-current multiphase 3-D integrated magnetics," *IEEE Trans. Power Electron.*, vol. 32, no. 11, pp. 8705–8717, Nov. 2017, doi: 10.1109/TPEL.2016.2646702.

[15] D. Dinulovic, M. Shousha, M. Haug, A. Gerfer, M. Wens, and J. Thone, "On-chip high performance magnetics for point-of-load high-frequency DC–DC converters," in *Proc. IEEE Appl. Power Electron. Conf. Expo. (APEC)*, Mar. 2016, pp. 3097–3100, doi: 10.1109/APEC.2016.7468306.

[16] W. J. Lambert, M. J. Hill, K. P. O'Brien, K. Radhakrishnan, and P. Fischer, "Study of thin-film magnetic inductors applied to integrated voltage regulators," *IEEE Trans. Power Electron.*, vol. 35, no. 6, pp. 6208–6220, Jun. 2020, doi: 10.1109/TPEL.2019.2948825.

[17] P. R. Morrow, C.-M. Park, H. W. Koertzen, and J. T. DiBene, "Design and fabrication of on-chip coupled inductors integrated with magnetic material for voltage regulators," *IEEE Trans. Magn.*, vol. 47, no. 6, pp. 1678–1686, Jun. 2011, doi: 10.1109/TMAG.2011.2116122.

[18] H. Jia, J. Lu, X. Wang, K. Padmanabhan, and Z. J. Shen, "Integration of a monolithic buck converter power IC and bondwire inductors with ferrite epoxy glob cores," *IEEE Trans. Power Electron.*, vol. 26, no. 6, pp. 1627–1630, Jun. 2011, doi: 10.1109/TPEL.2010.2100829.

[19] D. Yao, C. G. Levey, R. Tian, and C. R. Sullivan, "Microfabricated V-groove power inductors using multilayer Co–Zr–O thin films for very-high-frequency DC–DC converters," *IEEE Trans. Power Electron.*, vol. 28, no. 9, pp. 4384–4394, Sep. 2013, doi: 10.1109/TPEL.2012.2233760.

[20] D. V. Harburg *et al.*, "Measured performance and micro-fabrication of racetrack power inductors," in *Proc. IEEE Energy Convers. Congr. Expo.*, Sep. 2013, pp. 614–620, doi: 10.1109/ECCE.2013.6646758.

[21] S. L. Selvaraj *et al.*, "On-chip thin film inductor for high frequency DC–DC power conversion applications," in *Proc. IEEE Appl. Power Electron. Conf. Expo. (APEC)*, Mar. 2020, pp. 176–180, doi: 10.1109/APEC39645.2020.9124544.

[22] H. T. Le *et al.*, "High-Q three-dimensional microfabricated magnetic-core toroidal inductors for power supplies in package," *IEEE Trans. Power Electron.*, vol. 34, no. 1, pp. 74–85, Jan. 2019, doi: 10.1109/TPEL.2018.2847439.

[23] C. Feeney, N. Wang, S. Kulkarni, Z. Pavlovic, C. O. Mathuna, and M. Duffy, "Optimization of coupled stripline microinductors in power supply on chip applications," *IEEE Trans. Power Electron.*, vol. 31, no. 8, pp. 5805–5813, Aug. 2016, doi: 10.1109/TPEL.2015.2497968.

[24] M. Ludwig, M. Duffy, T. O'Donnell, P. McCloskey, and S. C. O. Mathuna, "PCB integrated inductors for low power DC/DC converter," *IEEE Trans. Power Electron.*, vol. 18, no. 4, pp. 937–945, Jul. 2003, doi: 10.1109/TPEL.2003.813757.

[25] L. Li *et al.*, "Small-resistance and high-quality-factor magnetic integrated inductors on PCB," *IEEE Trans. Adv. Packag.*, vol. 32, no. 4, pp. 780–787, Nov. 2009, doi: 10.1109/TADVP.2009.2019845.

[26] J. Lu, H. Jia, X. Wang, K. Padmanabhan, W. G. Hurley, and Z. J. Shen, "Modeling, design, and characterization of multiturn bondwire inductors with ferrite epoxy glob cores for power supply system-on-chip or system-in-package applications," *IEEE Trans. Power Electron.*, vol. 25, no. 8, pp. 2010–2017, Aug. 2010.

[27] W. J. Lambert, M. J. Hill, K. Radhakrishnan, L. Wojewoda, and A. E. Augustine, "Package inductors for Intel fully integrated voltage regulators," *IEEE Trans. Compon., Packag., Manuf. Technol.*, vol. 6, no. 1, pp. 3–11, Jan. 2016, doi: 10.1109/TCPMT.2015.2505665.

[28] N. Sturcken, R. Davies, C. Cheng, W. E. Bailey, and K. L. Shepard, "Design of coupled power inductors with crossed anisotropy magnetic core for integrated power conversion," in *Proc. 27th Annu. IEEE Appl. Power Electron. Conf. Expo. (APEC)*, Feb. 2012, pp. 417–423, doi: 10.1109/APEC.2012.6165853.

[29] S. Kulkarni, D. Li, D. Jordan, N. Wang, and C. O. Mathúna, "PCB embedded bondwire inductors with discrete thin-film magnetic core for power supply in package," *IEEE J. Emerg. Sel. Topics Power Electron.*, vol. 6, no. 2, pp. 614–620, Jun. 2018, doi: 10.1109/JESTPE.2018.2799238.

[30] M. L. F. Bellaredj, A. K. Davis, P. Kohl, and M. Swaminathan, "Magnetic core solenoid power inductors on organic substrate for system-in-package integrated high-frequency voltage regulators," *IEEE J. Emerg. Sel. Topics Power Electron.*, vol. 8, no. 3, pp. 2682–2695, Sep. 2020, doi: 10.1109/JESTPE.2019.2914215.

[31] T. Fukuoka *et al.*, "An 86% efficiency, 20 MHz, 3D-integrated buck converter with magnetic core inductor embedded in interposer fabricated by epoxy/magnetic-filler composite build-up sheet," in *Proc. IEEE Appl. Power Electron. Conf. Expo. (APEC)*, Mar. 2019, pp. 1561–1566, doi: 10.1109/APEC.2019.8722209.

[32] D. Jordan *et al.*, "High *Q*-factor PCB embedded flip-chip inductors with multilayer CZTB magnetic sheet for power supply in package (PwrSiP)," *IEEE J. Emerg. Sel. Topics Power Electron.*, vol. 9, no. 1, pp. 102–110, Feb. 2021, doi: 10.1109/JESTPE.2020.2983125.

[33] J. Qiu, D. V. Harburg, and C. R. Sullivan, "A toroidal power inductor using radial-anisotropy thin-film magnetic material based on a hybrid fabrication process," in *Proc. 28th Annu. IEEE Appl. Power Electron. Conf. Expo. (APEC)*, Mar. 2013, pp. 1660–1667, doi: 10.1109/APEC.2013.6520520.

[34] R. Murphy, Z. Pavlovic, P. McCloskey, C. O. Mathuna, S. O'Driscoll, and G. Weidinger, "PCB embedded toroidal inductor for 2 MHz point-of-load converter," in *Proc. 11th Int. Conf. Integr. Power Electron. Syst.*, Mar. 2020, pp. 1–5.

[35] Y. Sugawa, K. Ishidate, M. Sonehara, and T. Sato, "Carbonyl-iron/epoxy composite magnetic core for planar power inductor used in package-level power grid," *IEEE Trans. Magn.*, vol. 49, no. 7, pp. 4172–4175, Jul. 2013, doi: 10.1109/TMAG.2013.2250925.

[36] S.-T. Yang, C.-H. Chiang, Y.-C. Hsieh, P.-N. Lee, and C.-C. Wang, "PCB integrated inductor design optimized and electrical performance analysis for power module development," in *Proc. Electr. Design Adv. Packag. Syst. (EDAPS)*, Dec. 2019, pp. 1–3, doi: 10.1109/EDAPS47854.2019.9011673.

[37] C. Alvarez *et al.*, "Design and demonstration of single and coupled embedded toroidal inductors for 48 V to 1 V integrated voltage regulators," in *Proc. IEEE 70th Electron. Compon. Technol. Conf. (ECTC)*, Jun. 2020, pp. 405–413, doi: 10.1109/ECTC32862.2020.00072.

[38] C. Alvarez *et al.*, "Demonstration of a high-inductance, high-density, and low DC resistance compact embedded toroidal inductor for IVR," in *Proc. IEEE 71st Electron. Compon. Technol. Conf. (ECTC)*, Jun. 2021, pp. 1293–1299, doi: 10.1109/ECTC32696.2021.00209.

[39] Q. Li and F. C. Lee, "High inductance density low-profile inductor structure for integrated point-of-load converter," in *Proc. 24th Annu. IEEE Appl. Power Electron. Conf. Expo.*, Feb. 2009, pp. 1011–1017, doi: 10.1109/APEC.2009.4802786.

[40] Y. Su, D. Hou, F. C. Lee, and Q. Li, "Low profile coupled induc-tor substrate with fast transient response," in *Proc. IEEE Appl. Power Electron. Conf. Expo. (APEC)*, Mar. 2015, pp. 1161–1168, doi: 10.1109/APEC.2015.7104494.

[41] D. Hou, Y. Su, Q. Li, and F. C. Lee, "Improving the effi-ciency and dynamics of 3D integrated POL," in *Proc. IEEE Appl. Power Electron. Conf. Expo. (APEC)*, Mar. 2015, pp. 140–145, doi: 10.1109/APEC.2015.7104344.

[42] W. Zhang, Y. Su, M. Mu, D. J. Gilham, Q. Li, and F. C. Lee, "High-density integration of high-frequency high-current point-of-load (POL) modules with planar inductors," *IEEE Trans. Power Electron.*, vol. 30, no. 3, pp. 1421–1431, Mar. 2015, doi: 10.1109/TPEL.2014.2320857.

[43] Y. Su, W. Zhang, Q. Li, F. C. Lee, and M. Mu, "High frequency integrated point of load (POL) module with PCB embedded inductor substrate," in *Proc. IEEE Energy Convers. Congr. Expo.*, Sep. 2013, pp. 1243–1250, doi: 10.1109/ECCE.2013.6646847.

[44] Y. Su, Q. Li, and F. C. Lee, "FEA modeling of the low profile coupled inductor with non-uniform flux distribution," in *Proc. 28th Annu. IEEE Appl. Power Electron. Conf. Expo. (APEC)*, Mar. 2013, pp. 2416–2423, doi: 10.1109/APEC.2013.6520634.

[45] F. Zhu, Q. Li, and F. C. Lee, "Improved partial cancellation method for high frequency core loss measurement," in *Proc. IEEE Appl. Power Electron. Conf. Expo. (APEC)*, Mar. 2019, pp. 1430–1435, doi: 10.1109/APEC.2019.8722221.

[46] M. Mu, F. Zheng, Q. Li, and F. C. Lee, "Finite element analy-sis of inductor core loss under DC bias conditions," *IEEE Trans. Power Electron.*, vol. 28, no. 9, pp. 4414–4421, Sep. 2013, doi: 10.1109/TPEL.2012.2235465.

Feiyang Zhu (Graduate Student Member, IEEE) received the B.S. degree in electrical engineering from Wuhan University, Wuhan, China, in 2017. He is currently pursuing the Ph.D. degree with the Center for Power Electronics Systems, Virginia Polytechnic Institute and State University, Blacksburg, VA, USA.

His research interests include high-frequency magnetic components and high-frequency power conversion.

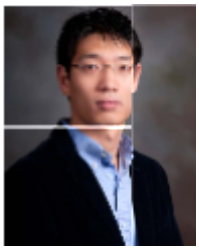

Qiang Li (Member, IEEE) received the B.S. and M.S. degrees in power electronics from Zhejiang University, Hangzhou, China, in 2003 and 2006, respectively, and the Ph.D. degree in electrical engineering from Virginia Polytechnic Institute and State University, Blacksburg, VA, USA, in 2011.

He is currently an Associate Professor with the Center for Power Electronics Systems, Virginia Polytechnic Institute and State University. His research interests include power management for distributed power systems, applications of wide-bandgap (WBG) power devices, high-frequency power conversion and controls, magnetics and electromagnetic interference (EMI), high-density electronics packaging and integration, and renewable energy.

Dr. Li was a recipient of the First Place Prize Paper Award for 2016 in the IEEE TRANSACTIONS ON POWER ELECTRONICS and the 2017 National Science Foundation (NSF) Career Award.